


RESEARCH ARTICLE | FEBRUARY 14 2024

Investigation of laser plasma instabilities driven by 527 nm laser pulses relevant for direct drive inertial confinement fusion

F. Wasser ; Ş. Zähler ; M. Rivers ; S. Atzeni ; F. P. Condamine ; G. Cristoforetti ; G. Fauvel ; N. Fischer ; L. A. Gizzi ; D. Hoffmann ; P. Koester ; T. Laštovička ; J. F. Myatt ; R. L. Singh ; M. Sokol ; W. Theobald ; S. Weber ; T. Ditmire ; T. Forner ; M. Roth

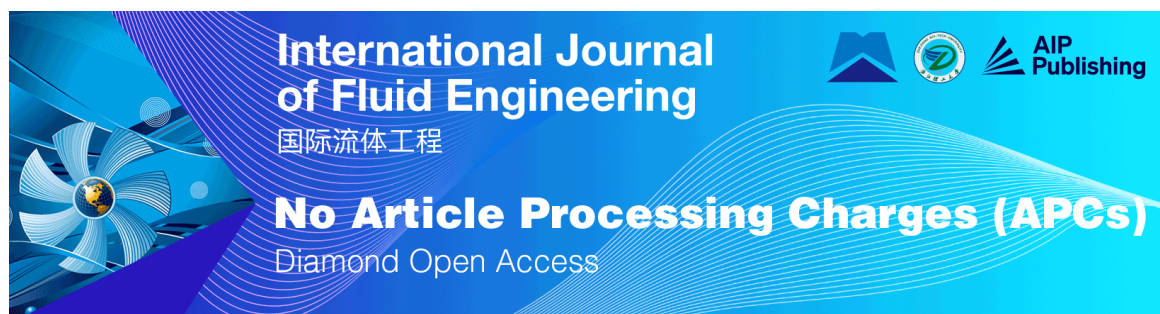
 Check for updates

Phys. Plasmas 31, 022107 (2024)

<https://doi.org/10.1063/5.0188693>




CrossMark



International Journal of Fluid Engineering
国际流体工程

No Article Processing Charges (APCs)
Diamond Open Access



Investigation of laser plasma instabilities driven by 527 nm laser pulses relevant for direct drive inertial confinement fusion

Cite as: Phys. Plasmas **31**, 022107 (2024); doi:10.1063/5.0188693

Submitted: 23 November 2023 · Accepted: 19 January 2024 ·

Published Online: 14 February 2024




View Online



Export Citation



CrossMark

F. Wasser,^{1,2,a)}  Ş. Zähler,¹  M. Rivers,³  S. Atzeni,¹  F. P. Condamine,⁴  G. Cristoforetti,⁵  G. Fauvel,⁴  N. Fischer,¹  L. A. Gizzi,⁵  D. Hoffmann,⁶  P. Koester,⁵ T. Laštovička,⁴ J. F. Myatt,⁷ R. L. Singh,⁴ M. Sokol,¹ W. Theobald,^{1,8} S. Weber,⁴ T. Ditmire,³ T. Forner,¹ and M. Roth^{1,9}

AFFILIATIONS

¹Focused Energy GmbH, Im Tiefen See 45, 64293 Darmstadt, Germany

²IU Internationale Hochschule GmbH, Darmstädter Landstrasse 110, 60598 Frankfurt am Main, Germany

³University of Texas, 110 Inner Campus Dr., Austin, Texas 78712, USA

⁴Extreme Light Infrastructure ERIC, ELI-Beamlines Facility, 25241 Dolní Břežany, Czech Republic

⁵Intense Laser Irradiation Laboratory, INO-CNR, Pisa, Italy

⁶Goethe University, Frankfurt, Max-von-Laue-Straße 1, 60438 Frankfurt am Main, Germany

⁷Department of Electrical and Computer Engineering, University of Alberta, 9211 116 St. NW, Alberta, Edmonton T6G 1H9, Canada

⁸Department of Mechanical Engineering, University of Rochester, Rochester, New York 14623, USA

⁹Technische Universität Darmstadt, Schlossgartenstrasse 9, 64289 Darmstadt, Germany

^{a)} Author to whom correspondence should be addressed: florian.wasser@focused-energy.world

ABSTRACT

We report on a study of laser plasma instabilities with 527 nm laser pulses in an intensity range of $0.5 \times 10^{13} - 1.1 \times 10^{15} \text{ Wcm}^{-2}$ and plasma parameters entering a regime that is relevant for direct drive inertial confinement fusion. Using the kilojoule high repetition rate L4n laser at the Extreme Light Infrastructure—Beamlines, more than 1300 shots were collected, and the onset and the growth of stimulated Brillouin scattering (SBS) and stimulated Raman scattering (SRS) were studied with a high confidence level. The measured onset intensities are $0.2 \times 10^{14} \text{ Wcm}^{-2}$ for SBS and $1.4 \times 10^{14} \text{ Wcm}^{-2}$ for SRS. At the maximum intensity, the total fraction of backscattered energy reaches 2.5% for SBS and 0.1% for SRS. These results are of high relevance for advanced concepts for inertial fusion energy, which rely on the use of 527 nm laser light to drive the implosion of the fuel target, and in particular, they can be used as a benchmark for advanced simulations.

© 2024 Author(s). All article content, except where otherwise noted, is licensed under a Creative Commons Attribution-NonCommercial 4.0 International (CC BY-NC) license (<http://creativecommons.org/licenses/by-nc/4.0/>). <https://doi.org/10.1063/5.0188693>

I. INTRODUCTION

More than 60 years of research in inertial confinement fusion (ICF) came to fruition with the recent demonstration of ignition and net energy gain at the National Ignition Facility (NIF).¹ This result strongly supports the work of several recently founded startup companies that pursue the goal to commercialize fusion energy within a few decades.² The step from understanding the fundamentals toward an actual power plant sets additional requirements and constraints. In particular, the fusion energy gain must be high enough to compensate for the electrical energy consumption of the plant, stable long-term operation must be ensured, and operational costs of the facility must be kept low. The recently established company Focused Energy has

presented a concept to address these requirements.³ One aspect is the use of laser light with a wavelength of 527 nm to compress the fusion pellets, which will be discussed below.

In ICF,^{4,5} lasers with intensities in the range $1 \times 10^{14} - 1 \times 10^{15} \text{ Wcm}^{-2}$ are used to drive the implosion of a capsule, which contains the fuel in order to achieve sufficient areal density, hotspot temperature, and confinement time required by the well-known Lawson criterion.⁶ At these intensities, a plasma corona is formed at the target surface with a density scale length that is typically of the order of several $100 \mu\text{m}$ and an electron temperature around a few keV. Under these conditions, the laser field can couple to electron and ion-acoustic plasma waves and coherently transfer energy to the growing plasma

waves and scattered light waves.⁷ The various laser plasma instability (LPI) mechanisms are usually classified based on the participating waves. Most relevant for ICF are stimulated Brillouin scattering (SBS), cross-beam energy transfer (CBET),⁸ stimulated Raman scattering (SRS),⁹ and two plasmon decay (TPD).^{7,10–13} TPD is the decay of an incoming laser photon into two electron plasma waves, SRS is the decay of a laser photon into an electron plasma wave and a scattered photon, and SBS is the decay of a laser photon into an ion-acoustic wave and a scattered photon. CBET is the energy transfer from one laser beam to another intercepting beam in the plasma corona, when ion-acoustic waves are driven resonantly. All these effects are detrimental to ICF because they can significantly impact the implosion through reduced laser-energy coupling, increased illumination non-uniformity, and hot electron preheat.^{14–17}

So far, the ICF community has preferred shorter wavelengths for the compression pulses because of an improved laser-target coupling, higher ablation pressure for a given intensity, and reduced LPIs.^{18,19} In particular, the primary absorption mechanism is collisional absorption,²⁰ which is more effective at shorter wavelengths, since the laser can propagate to higher densities where the collision rate is larger. Therefore, existing ICF research facilities like the NIF,²¹ OMEGA,²² and the Laser MegaJoule (LMJ)²³ operate at a wavelength of 351 nm, the third harmonic (3ω) of the 1053 nm fundamental (1ω) of Nd:glass lasers. On the other hand, there are considerable advantages of longer wavelengths for an actual ICF power plant, which is why Focused Energy is pursuing the commercialization of inertial fusion energy using 527 nm (2ω) laser light for compression of spherical cryogenic deuterium–tritium targets.⁵ The main advantages of 2ω light compared to 3ω are higher damage thresholds of optics, more available laser energy, and potentially larger spectral bandwidth, which is important for laser smoothing techniques and mitigation of LPIs. Unlike at existing facilities where frequency conversion is done close to the target chamber in order to minimize the number of transport optics for 351 nm light, the frequency conversion optics can be installed directly after the final amplifier. This reduces the costs for the beam transport and prevents the damage risk for high value frequency conversion optics due to the harsh conditions (e.g., the high neutron flux) close to the interaction point. This option is supported by recent progress in LPI mitigation techniques,^{24–26} which could help to overcome the drawback of lower LPI intensity threshold at longer wavelengths.

While much work has been done to characterize LPIs with 351 nm light especially at NIF and OMEGA,^{27–31} experimental data with 527 nm light are scarce. Especially with the focus on the direct drive approach, which is considered beneficial for commercial fusion energy because of a higher laser to target coupling efficiency compared to indirect drive,³ only a few relevant experimental studies of LPIs with 2ω light can be found. Some early work on SRS has been done by Turner *et al.*³² in the 1980s. By irradiating Au and Be disk targets with up to 150 J with 0.9 ns pulses focused to a 75 μm spot size, they observed broad SRS spectra in the 700–900 nm range, which were predominant in backscatter direction with a total energy fraction of 10^{-4} with respect to the incident laser energy. In a later work, Turner *et al.*³³ observed less SRS using a 260 nm laser driver compared to a 530 nm laser. This effect was significantly more pronounced in gold (Au) targets compared to plastic (CH) targets, which was explained by collisional damping of the Raman instability in high-Z targets. Additional SRS measurements with flat Au targets and laser intensities

in the $1 \times 10^{14} - 1 \times 10^{16} \text{Wcm}^{-2}$ range were done by Drake *et al.* in the 1980s.^{34,35} The main observations were broad spectra in the 750–950 nm range, a fast growth of the SRS fluence over three orders of magnitude when the laser intensity was increased from 1×10^{14} to $2 \times 10^{15} \text{Wcm}^{-2}$. It was observed that the SRS fluence saturates for higher intensities. Furthermore, the measured SRS signal was maximal in backscatter direction (180°) with some sidescatter contribution up to 120° . SBS has been studied with 527 nm in comparison to 351 nm laser pulses by Depierreux *et al.* in 2009 and 2012.^{36,37} Using planar CH targets, they observed similar saturation levels around 10% for both wavelengths and an onset of SRS at $3 \times 10^{14} \text{Wcm}^{-2}$ with 527 nm light and at $5 \times 10^{14} \text{Wcm}^{-2}$ with 351 nm light.

For the experiments mentioned above, the number of data points was strongly limited due to the low repetition rates of the used laser systems. In this article, we report on an extensive study of SBS and SRS with 527 nm laser pulses in an intensity range of $0.5 \times 10^{13} - 1.1 \times 10^{15} \text{Wcm}^{-2}$ and plasma conditions with a density scale length of about 200 μm and an electron temperature of 1–2 keV with more than 1300 shots. Even though the density scale length and electron temperature in the corona are about a factor of 3 lower than in an ignition target, the coronal plasma conditions are approaching the regime that is relevant for direct drive ICF. The onset and the growth of the instabilities were measured with a high confidence level. A narrow spectral bandwidth laser was used in the experiment, and it is expected that the results give a lower limit of the laser intensity thresholds for the onset of SBS and SRS for a given set of plasma parameters. It is predicted that broad spectral bandwidth light will mitigate LPI leading to higher thresholds.

II. EXPERIMENTAL SETUP

The experiment was performed at the recently commissioned high repetition rate, nanosecond, kilojoule L4n laser at the Extreme Light Infrastructure (ELI)—Beamlines.^{38–40} A schematic of the experimental setup is shown in Fig. 1. Planar solid targets were irradiated with frequency doubled light at varying intensities. The targets were 200 μm thick polyvinyl chloride (PVC) foils, and the laser was incident at 7° with respect to the target normal direction to minimize harmful back reflections. While the L4n beamline nominally operates at a fundamental wavelength of 1053 nm, we used a KDP crystal to convert to the second harmonic with a wavelength of 527 nm. Square pulse shaped laser pulses with a duration between 2 and 2.5 ns were used. The focal spot diameter was 110 μm (FWHM). We scanned the laser energy from 0.1 to 220 J, corresponding to an intensity range of $0.5 \times 10^{13} - 1.1 \times 10^{15} \text{Wcm}^{-2}$. A dataset of over 1300 shots was collected during the experimental campaign, thanks to the exceptionally high repetition rate of the system.

LPIs were measured and characterized using a full aperture backscatter diagnostic (BSD) station,⁴¹ which was recently commissioned at ELI.⁴² A fraction of the light scattered back from the target leaks through the final turning mirror in front of the target chamber and is subsequently transported to the BSD where it is split into different channels for back scattered energy measurement, detection of the SBS and SRS signals, as well as measurement of the $3/2\omega$ signal from TPD. The SBS and SRS signals are measured spectrally and temporally resolved using two Czerny–Turner spectrographs, which are coupled to two streak cameras. In addition, two calorimeters with spectral filters were used to measure the total energy of the backscattered SBS and SRS signals, respectively. The TPD signal is measured temporally

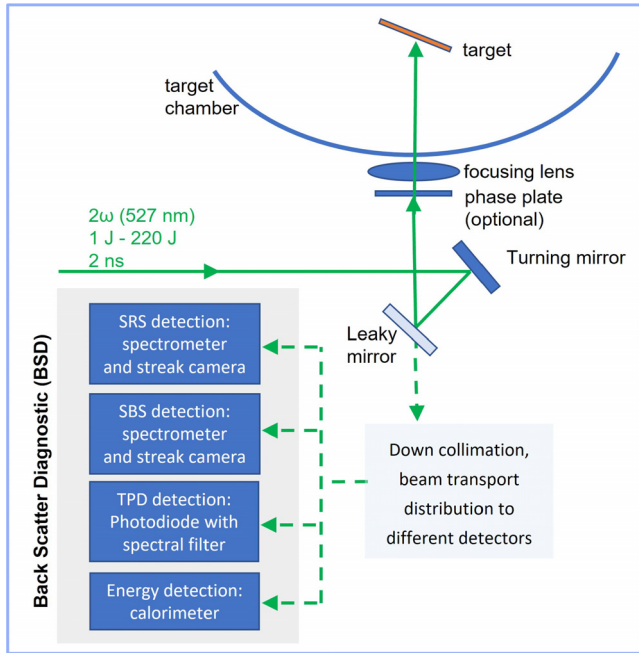


FIG. 1. Schematic drawing of the setup of the backscatter diagnostics. See text for details.

resolved using a high speed photo diode with a rise time shorter than 300 ps and a 44 nm bandpass filter centered around 357 nm in front of the photo diode. A detailed description of the diagnostic and its commissioning at ELI is given in Ref. 42.

III. RESULTS

Time resolved SRS and SBS spectra from a shot with 94 J, a laser pulse duration of 2.4 ns and an intensity of $4 \times 10^{14} \text{ Wcm}^{-2}$ are shown in Fig. 2. The spectral shift and broadening for both SBS and SRS match results from comparable experiments conducted at other facilities.^{20,37,43} The central wavelength of the SBS signal is close to the laser wavelength and the integrated bandwidth is around 1.4 nm. The total temporal duration of the signal is 2.3 ns (FWHM) which is close to the laser pulse duration, showing that at this laser intensity SBS occurs for the bulk of the laser-plasma interaction. It is worth noting that while the signal starts growing smoothly at the beginning, it stops more

abruptly at the end of the interaction. This can be explained by the need for the plasma to evolve first before the ion-acoustic plasma wave can start to grow and induce SBS. On the other hand, SBS stops immediately, when the laser intensity drops below the threshold intensity for SBS at the tail of the laser pulse. The spectral maximum is at the laser wavelength of 527 nm at the beginning of the interaction, and it is then rapidly shifted to 526.5 nm within the first 200 ps where it stays till the end. This blueshift can be explained by SBS growing in a plasma that expands toward the incident laser.³⁶ The constant wavelength shift after 200 ps indicates that the plasma flow velocity has reached a steady state after that time. This is also in agreement with 2D radiation hydrodynamic simulations which will be discussed in Sec. IV.

Comparable to other experiments,²⁰ we observe a significant redshift and broadening of the SRS signal. The total signal ranges over about 80 nm from 750 to 830 nm. This corresponds to SRS driven in an electron density range of $n_e \approx 0.09 n_c$ to $n_e \approx 0.13 n_c$, where n_c denotes the critical density for a wavelength of 527 nm. As discussed in Ref. 44, this observed limitation of the density range where SRS takes place can be explained by an interplay between collisional damping and Landau damping through the variation of the damping rates with plasma density. While Landau damping limits the spectrum at short wavelength (low densities), collisional damping limits it at long wavelength (high densities). Like the SBS signal, also the SRS signal breaks off abruptly. Since this can be attributed to the end of the laser pulse for both SBS and SRS, the offsets of the not absolutely calibrated time axes were set to show the turn-offs of the SBS and SRS signals at the same time in Fig. 2. The total temporal window within which a SRS signal above the noise level was detected at this shot is 1.8 ns and the FWHM of this signal is only 1.1 ns (FWHM). In contrast to SBS, this is much shorter than the laser pulse duration. This difference can be explained by the different evolution of the intensity thresholds for SBS and SRS, which will be discussed in Sec. IV.

The variation of absolute and relative SBS and SRS energies with increasing laser intensity are shown in Figs. 3 and 4. The figures include the calorimeter data as well as time and wavelength integrated signals from the streak camera images, which were rescaled to match the absolute energy values measured with the calorimeter. Thanks to the higher sensitivity of the streak cameras, this allows to inspect the trends of data points in the lower laser intensity range, where the SBS and SRS signals were below the detection threshold of the calorimeters. We observe a rapid growth of the SBS energy over three orders of magnitude within the laser intensity range from 2×10^{13} to $1 \times 10^{14} \text{ Wcm}^{-2}$. At this intensity, the total SBS reflectivity reaches a value of about 1%

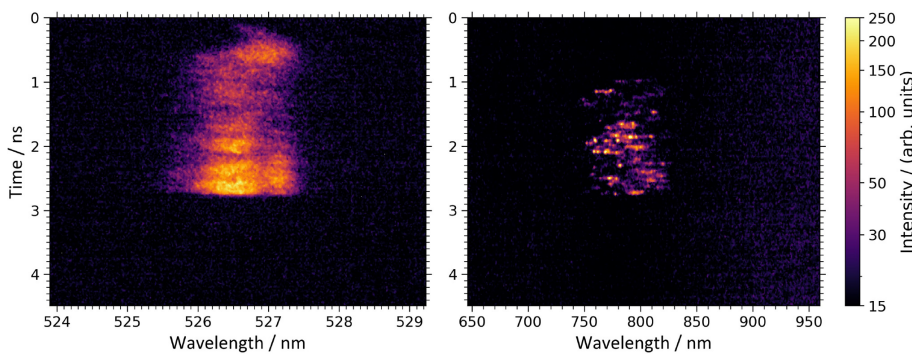


FIG. 2. Time resolved SBS spectrum (left) and SRS spectrum (right) from a shot with 94 J laser energy, a laser pulse duration of 2.4 ns, and an intensity of $4 \times 10^{14} \text{ Wcm}^{-2}$. Because of the lack of a timing fiducial, the time axis were adjusted such that the signal falling edge of the SBS and SRS pulses were aligned with the falling edge of the laser pulse.

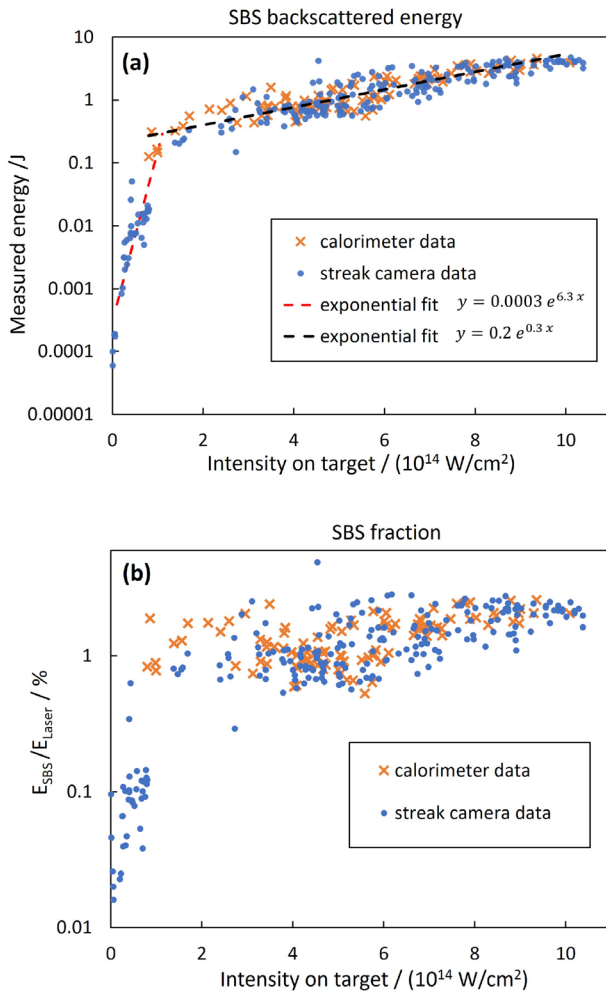


FIG. 3. Backscattered SBS energy measured with a calorimeter (orange crosses) and from the integration and rescaling of the streak camera images over time and wavelength (blue points). In (a), the absolute energy values are shown, and in (b), the energy fraction with respect to the incoming laser energy is shown.

[see Fig. 3(b)]. For higher laser intensities, the SBS signal continues growing exponentially but with a lower exponent [compare exponential fits in Fig. 3(a)]. At an intensity of $1.1 \times 10^{15} \text{ Wcm}^{-2}$, a total reflected energy fraction of 2.5% is reached.

The SRS signals (see Fig. 4) show a similar general behavior with a fast growing at the beginning which turns abruptly into a slower growth. However, the onset of the instability is observed at a higher intensity of $1.4 \times 10^{14} \text{ Wcm}^{-2}$ and the change of slope appears at $3 \times 10^{14} \text{ Wcm}^{-2}$. At this intensity, the total reflected energy fraction is 0.01% and it reaches about 0.1% at the intensity of $1.1 \times 10^{15} \text{ Wcm}^{-2}$.

A possible explanation for the rapid onset of the LPI signals with intensity at the beginning, which turns abruptly into a slower growth for higher intensities is given by a theoretical study by Vu *et al.* in 2007.⁴⁵ According to this theory, LPIs first start to grow in speckles or hot spots of the laser pulse profile, where the intensity exceeds the average intensity. The generated waves can then seed LPIs in other

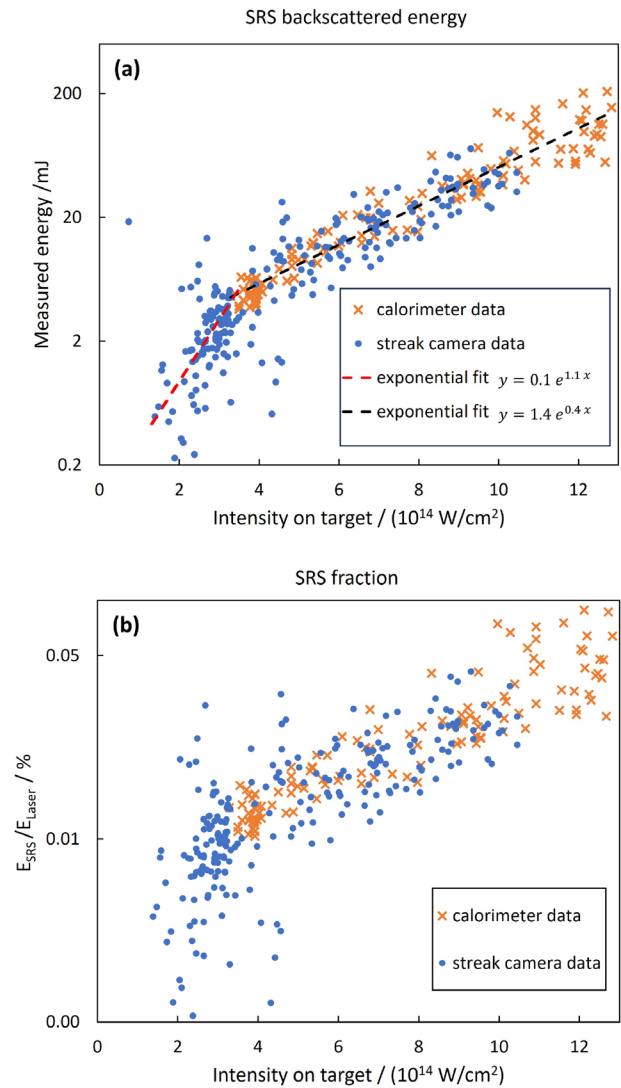


FIG. 4. Backscattered SRS energy measured with a calorimeter (orange crosses) and from the integration and rescaling of the streak camera images over time and wavelength (blue points). In (a), the absolute energy values are shown, and in (b), the energy fraction with respect to the incoming laser energy is shown.

speckles leading to a rapid onset of the overall instability at a critical intensity. For SRS, this effect can be enhanced by the onset of electron trapping in the laser speckles which Vu *et al.* call inflation threshold.

IV. SIMULATIONS AND DISCUSSIONS

In this section the measured onset of SBS and SRS is compared with single beam intensity thresholds from Refs. 46 and 47. At these intensities, the growth rate surpasses the loss rates from wave damping and the plasma wave starts to grow exponentially. In Eqs. (1) and (2), the intensity thresholds are given in units of $1 \times 10^{14} \text{ Wcm}^{-2}$, L_{ne} is the electron density scale length in units of micrometer, λ is the laser wavelength in units of micrometer, T_e is the electron temperature in units of keV, L_ν is the scale length of the Mach number profile (plasma

flow) in units of micrometer, n_c is the critical density, and n_e is the electron density.

$$I_{thr}(SRS) \approx 900 \frac{1}{L_{ne}^{4/3} \lambda^{2/3}}, \quad (1)$$

$$I_{thr}(SBS) \approx 70 \frac{T_e}{L_{ne} \lambda} \frac{n_c}{n_e}. \quad (2)$$

It should be noted here, that in the literature, Eq. (1) is usually only used for absolute SRS or side scatter SRS, while for convective backscatter SRS another formula is used, where the intensity threshold scales as $\frac{1}{L_{ne} \lambda}$.⁴⁸ However, as discussed in Ref. 7, the latter formula only applies for densities $n_e \ll n_{cr}/4$. For higher densities as in this experiment, a correction factor must be applied and the scaling becomes as in Eq. (1).

The formulas show that for higher wavelength both instabilities start to grow at lower laser intensities, confirming that LPs are more critical for 2ω light compared to 3ω light. To calculate the intensity thresholds for this experiment, the plasma parameters for our laser and target conditions were simulated with the 2D radiation hydrodynamic code DUED.⁴⁹ The code describes laser heating by using ray-tracing, with the classical dispersion relation for electromagnetic waves in a plasma and collisional absorption. The temporal pulse profile of the 2 ns long pulses was modeled with a trapezoidal shape with a 0.1 ns long ramp up followed by a plateau and a 0.1 ns long ramp down to zero. For the focal spot, a Gaussian distribution was used with a FWHM of 110 μm .

An example for simulated plasma parameters for a laser energy of 200 J and an intensity of $1 \times 10^{15} \text{Wcm}^{-2}$ evaluated after 1 ns is shown in Fig. 5. The parameter z denotes the axial distance from the target. The target front surface was initially placed at $z = 200 \mu\text{m}$. The electron density shows a typical exponential decay in the underdense region with a scale length of about 170 μm at a density of $0.1n_c$. The electron temperature peaks at a value around 1.8 keV at the critical density and drops to 1.6 keV at quarter critical density and to 1.3 keV at $0.1n_c$. In this region, the plasma flow velocity is positive, showing that the plasma flows from the target in the direction toward the laser. The flow velocity increases slowly for higher distances from the target surface with a scale length of about 400 μm at $0.1n_c$.

The absorbed laser energy fraction at different locations in the plasma can be retrieved from the simulation. In the region up to $n_c/4$, which is most relevant for the observed LPs, typically around 20% of the laser energy is absorbed, while most of the absorption (up to 80%)

happens in the higher density region between $n_c/4$ and n_c . This shows a minor depletion of the driving laser wave from collisional absorption, which will not significantly affect the onset and generation of LPs. On the other hand, the scattered waves can also be re-absorbed in the plasma through collisional absorption. The collisional absorption coefficient can be calculated with the standard formula as given in Ref. 50. For the plasma conditions of our experiment, we estimate absorption coefficients of $\kappa_{SBS} \approx 3 \times 10^{-4} \mu\text{m}$ for SBS and $\kappa_{SRS} \approx 8 \times 10^{-4} \mu\text{m}$ for SRS. This corresponds to an absorption of about 5% for the SBS wave and 13% for the SRS wave over the scale length of 170 μm .

Simulations were done for three different laser intensities 0.5×10^{14} , 2.6×10^{14} , and $5.3 \times 10^{14} \text{Wcm}^{-2}$. As in the experiment, the laser intensity was varied in the simulation by changing the laser energy while keeping the spot size and pulse duration fixed. For the calculation of the threshold intensities for SBS and SRS, the plasma parameters were retrieved for different time steps during the laser-target interaction. Figure 6 shows the evolution of the ratio of the laser intensity and the calculated threshold intensities for SBS and SRS. When this value exceeds 1, the laser intensity is above threshold and the instability can start to grow.

All curves rise fast in the first few 100 ps due to the ramp up of the laser intensity and the formation of the plasma. As the laser plateau is reached, the SRS threshold continues decreasing due to the ongoing growth of the electron density scale length L_{ne} . Similarly, the SBS thresholds continue decreasing because the plasma flow velocity scale length increases. In the last 100 ps, all curves drop rapidly due to the ramp down of the laser intensity. For $0.5 \times 10^{14} \text{Wcm}^{-2}$, the intensity stays below the SRS threshold during the interaction while the SBS threshold is just reached but not exceeded for a duration of about 1.5 ns. For $2.6 \times 10^{14} \text{Wcm}^{-2}$, the SRS and SBS thresholds are passed after 0.8 and 0.15 ns, respectively. As expected, for the intensity of $5.3 \times 10^{14} \text{Wcm}^{-2}$, the thresholds are passed at earlier times, after 0.4 ns for SRS and 0.1 ns for SBS. These simulation results explain the temporal features of the SRS and SBS signals observed in the experiment with a smooth growth in the beginning, a rapid drop at the end, and a longer duration of the SBS signal compared to the SRS signal. Remarkably, the measured duration of the signals for the discussed case with an intensity of $4 \times 10^{14} \text{Wcm}^{-2}$ (see Fig. 2) and time windows during which the intensity thresholds are exceeded for a simulated intensity of $2.6 \times 10^{14} \text{Wcm}^{-2}$ fit quite well.

From the simulations, the onset of the instabilities would be expected around $0.5 \times 10^{14} \text{Wcm}^{-2}$ for SBS and around $2 \times 10^{14} \text{Wcm}^{-2}$ for SRS. Both is about a factor of two higher than the experimentally observed

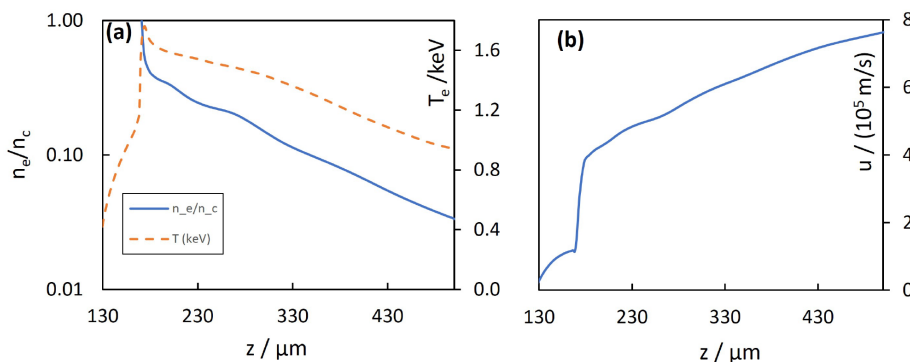


FIG. 5. Plasma parameters from 2D radiation hydrodynamic simulations for a square pulse with 2 ns duration, a laser energy of 200 J and an intensity of $1 \times 10^{15} \text{Wcm}^{-2}$ evaluated after 1 ns. The parameters are calculated along the symmetry axis of the simulation. In (a), the blue line shows the electron density normalized to the critical density for 527 nm and the orange dashed line shows the electron temperature. In (b), the plasma flow velocity is shown.

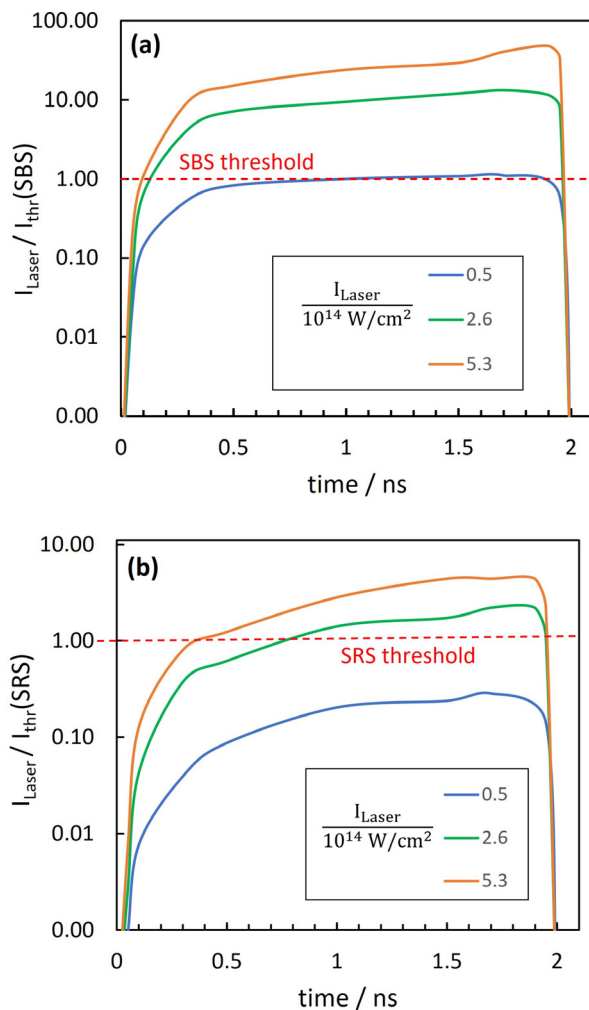


FIG. 6. Ratio of the laser intensity and the calculated threshold intensities for SBS (a) and SRS (b) for three different laser intensities.

onset intensities as discussed above. This difference could be attributed to an inhomogeneous intensity distribution in the focal spot. An analysis of the focal spot profile shows that there are hot spots with intensities around 2 times higher than the average intensity. Hence, the intensity thresholds are first exceeded in these hotspots, triggering the instabilities already at average intensities that are a factor of two lower than the calculated threshold.

V. CONCLUSION

Thanks to the high repetition rate of the ELI L4n laser, we have collected a conclusive dataset for backscattered SBS and SRS with 527 nm laser pulses for conditions that are approaching a regime that is relevant for ICF. The onsets and the growth of the instabilities with increasing laser intensity are measured with a high confidence level, and the onsets are consistent with the performed 2D hydrodynamic simulations. This dataset fills the gap of scarce ICF relevant LPI data with 527 nm laser light and is of high relevance for advanced inertial

fusion energy (IFE) concepts relying on frequency doubled pulses. It should be noted that the onset intensities for LPIs in actual IFE designs are expected to be lower than those presented in this study because of the considerably larger density gradient scale length of reactor-size targets. However, the data are of great value since they provide a good basis for further upscaling calculations. In particular, the dataset presented in this paper will be used as a benchmark for extensive LPI simulations in the future. Furthermore, the study shows that with 527 nm laser pulses, even at the given scale length of the order of 200 μm , SBS and SRS thresholds are exceeded for intensities in the range of $1 \times 10^{14} - 1 \times 10^{15} \text{ Wcm}^{-2}$. This stresses the need to consider LPI mitigating techniques such as applying increased laser bandwidth.²⁴ It is predicted that broad spectral bandwidth light will mitigate LPI leading to higher thresholds. Future experiments are planned to study LPI with 2ω broad spectral bandwidth light.

AUTHOR DECLARATIONS

Conflict of Interest

The authors have no conflicts to disclose.

Author Contributions

F. Wasser: Conceptualization (lead); Data curation (lead); Formal analysis (lead); Investigation (lead); Methodology (lead); Project administration (lead); Supervision (lead); Validation (lead); Visualization (equal); Writing – original draft (lead); Writing – review & editing (lead). **Ş. Zähler:** Conceptualization (equal); Data curation (equal); Formal analysis (equal); Investigation (equal); Methodology (equal); Writing – original draft (supporting); Writing – review & editing (supporting). **M. RIVERS:** Conceptualization (supporting); Data curation (equal); Investigation (supporting); Methodology (supporting). **S. Atzeni:** Formal analysis (supporting); Investigation (supporting); Software (equal); Writing – review & editing (supporting). **F. P. Condamine:** Data curation (supporting); Investigation (supporting); Methodology (supporting). **G. Cristoforetti:** Conceptualization (supporting); Investigation (supporting); Validation (supporting); Writing – review & editing (supporting). **G. Fauvel:** Data curation (supporting). **N. Fischer:** Formal analysis (supporting); Investigation (supporting); Writing – original draft (supporting); Writing – review & editing (supporting). **L. A. Gizzi:** Conceptualization (supporting); Investigation (supporting); Methodology (supporting); Resources (supporting); Validation (supporting). **D. Hoffmann:** Formal analysis (supporting); Software (supporting). **P. Koester:** Data curation (supporting). **T. Lastovicka:** Data curation (supporting); Investigation (supporting); Writing – review & editing (equal). **J. F. Myatt:** Investigation (supporting); Software (supporting). **R. L. Singh:** Data curation (supporting); Investigation (supporting). **M. Sokol:** Methodology (supporting); Resources (supporting); Software (supporting); Writing – review & editing (supporting). **W. Theobald:** Conceptualization (equal); Data curation (equal); Formal analysis (equal); Investigation (equal); Resources (equal); Supervision (equal); Validation (equal); Writing – original draft (supporting); Writing – review & editing (equal). **S. Weber:** Conceptualization (equal); Investigation (supporting); Project administration (equal); Resources (equal); Supervision (equal); Writing – review & editing (equal). **T. Ditmire:** Conceptualization (supporting); Funding acquisition (equal); Resources (equal); Supervision (equal). **T. Forner:** Funding acquisition (lead); Resources (equal). **M. Roth:** Conceptualization (supporting);

Formal analysis (supporting); Funding acquisition (lead); Investigation (supporting); Methodology (supporting); Resources (lead); Supervision (equal); Validation (equal); Writing – review & editing (supporting).

DATA AVAILABILITY

The data that support the findings of this study are available from the corresponding author upon reasonable request.

REFERENCES

- ¹H. Abu-Shawareb, R. Acree, P. Adams, J. Adams, B. Addis, R. Aden, P. Adrian, B. B. Afeyan, M. Aggleton, L. Aghaian *et al.*, *Phys. Rev. Lett.* **129**, 075001 (2022).
- ²Fusion Industry Association, see <https://www.fusionindustryassociation.org> for “The global fusion industry in 2023 (2023).”
- ³T. Ditmire, M. Roth, P. K. Patel, D. Callahan, G. Cheriaux, P. Gibbon, D. Hammond, A. Hannasch, L. C. Jarrott, G. Schaumann *et al.*, *J. Fusion Energy* **42**, 27 (2023).
- ⁴J. Nuckolls, L. Wood, A. Thiessen, and G. Zimmerman, *Nature* **239**, 139–142 (1972).
- ⁵S. Atzeni and J. Meyer-ter-Vehn, *The Physics of Inertial Fusion* (Clarendon, 2004).
- ⁶J. D. Lawson, *Proc. Phys. Soc., London* **70**, 6 (1957).
- ⁷W. L. Kruer, *The Physics of Laser Plasma Interactions* (Addison-Wesley, Redwood City, CA, 1988).
- ⁸I. V. Igumenshchev, W. Seka, D. H. Edgell, D. T. Michel, D. H. Froula, V. N. Goncharov, R. S. Craxton, L. Divol, R. Epstein, R. Follett *et al.*, *Phys. Plasmas* **19**, 056314 (2012).
- ⁹D. W. Phillion, D. L. Banner, E. M. Campbell, R. E. Turner, and K. G. Estabrook, *Phys. Fluids* **25**, 1434 (1982).
- ¹⁰A. Simon, R. W. Short, E. A. Williams, and T. Dewandre, *Phys. Fluids* **26**, 3107 (1983).
- ¹¹W. Seka, E. A. Williams, R. S. Craxton, L. M. Goldman, R. W. Short, and K. Tanaka, *Phys. Fluids* **27**, 2181 (1984).
- ¹²K. Tanaka, L. M. Goldman, W. Seka, M. C. Richardson, J. M. Soures, and E. A. Williams, *Phys. Rev. Lett.* **48**, 1179 (1982).
- ¹³A. I. Avrov, V. I. Bychenkov, O. N. Krokhin, V. V. Pustovalov, A. A. Rupasov, V. P. Silin, G. V. Sklizkov, V. T. Tikhonchuk, and A. S. Shikanov, *Sov. Phys.-JETP* **45**, 507 (1977).
- ¹⁴B. Yaakobi, P.-Y. Chang, A. Solodov, C. Stoeckl, D. H. Edgell, R. S. Craxton, S. X. Hu, J. F. Myatt, F. J. Marshall, W. Seka, and D. H. Froula, *Phys. Plasmas* **19**, 012704 (2012).
- ¹⁵B. Yaakobi, C. Stoeckl, T. Boehly, D. D. Meyerhofer, and W. Seka, *Phys. Plasmas* **7**, 3714 (2000).
- ¹⁶V. A. Smalyuk, D. Shvarts, R. Betti, J. A. Delettrez, D. H. Edgell, V. Y. Glebov, V. N. Goncharov, R. L. McCrory, D. D. Meyerhofer, P. B. Radha *et al.*, *Phys. Rev. Lett.* **100**, 185005 (2008).
- ¹⁷A. A. Solodov, M. J. Rosenberg, M. Stoeckl, A. R. Christopherson, R. Betti, P. B. Radha, C. Stoeckl, M. Hohenberger, B. Bachmann, R. Epstein *et al.*, *Phys. Rev. E* **106**, 055204 (2022).
- ¹⁸E. A. Fabre, *Plasma Phys. Controlled Nucl. Fusion Res.* **2**, 263–272 (1980).
- ¹⁹A. J. Schmitt and S. Obenschain, *Phys. Plasmas* **30**, 012702 (2023).
- ²⁰R. S. Craxton, K. S. Anderson, T. R. Boehly, V. N. Goncharov, D. R. Harding, J. P. Knauer, R. L. McCrory, P. W. McKenty, D. D. Meyerhofer, J. F. Myatt *et al.*, *Phys. Plasmas* **22**, 110501 (2015).
- ²¹E. M. Campbell and W. J. Hogan, *Plasma Phys. Controlled Fusion* **41**, B39 (1999).
- ²²T. Boehly, D. Brown, R. Craxton, R. Keck, J. Knauer, J. Kelly, T. Kessler, S. Kumpan, S. Loucks, S. Letzring *et al.*, *Opt. Commun.* **133**, 495 (1997).
- ²³M. L. André, *Fusion Eng. Des.* **44**, 43 (1999).
- ²⁴R. K. Follett, J. G. Shaw, J. F. Myatt, H. Wen, D. H. Froula, and J. P. Palastro, *Phys. Plasmas* **28**, 032103 (2021).
- ²⁵J. W. Bates, J. F. Myatt, J. G. Shaw, R. K. Follett, J. L. Weaver, R. H. Lehmburg, S. P. Obenschain *et al.*, *Phys. Rev. E* **97**, 061202 (2018).
- ²⁶B. J. Albright, L. Yin, and B. Afeyan, *Phys. Rev. Lett.* **113**, 045002 (2014).
- ²⁷D. H. Froula, B. Yaakobi, S. X. Hu, P.-Y. Chang, R. S. Craxton, D. H. Edgell, R. Follett, D. T. Michel, J. F. Myatt, W. Seka *et al.*, *Phys. Rev. Lett.* **108**, 165003 (2012).
- ²⁸W. Seka, D. H. Edgell, J. F. Myatt, A. V. Maximov, R. W. Short, V. N. Goncharov, and H. A. Baldis, *Phys. Plasmas* **16**, 052701 (2009).
- ²⁹M. J. Rosenberg, A. A. Solodov, J. F. Myatt, W. Seka, P. Michel, M. Hohenberger, R. W. Short, R. Epstein, S. P. Regan, E. M. Campbell *et al.*, *Phys. Rev. Lett.* **120**, 055001 (2018).
- ³⁰A. R. Christopherson, R. Betti, C. J. Forrest, J. Howard, W. Theobald, J. A. Delettrez, M. J. Rosenberg, A. A. Solodov, C. Stoeckl, D. Patel *et al.*, *Phys. Rev. Lett.* **127**, 055001 (2021).
- ³¹J. D. Moody, P. Datte, K. Krauter, E. Bond, P. A. Michel, S. H. Glenzer, L. Divol, C. Niemann, L. Suter, N. Meezan *et al.*, *Rev. Sci. Instrum.* **81**, 10D921 (2010).
- ³²R. E. Turner, D. W. Phillion, E. M. Campbell, and K. Estabrook, *Phys. Fluids* **26**, 579–581 (1983).
- ³³R. E. Turner, K. Estabrook, R. L. Kauffman, D. R. Bach, R. P. Drake, D. W. Phillion, B. F. Lasinski, E. M. Campbell, W. L. Kruer, and E. A. Williams, *Phys. Rev. Lett.* **54**, 189 (1985).
- ³⁴R. P. Drake, R. E. Turner, B. F. Lasinski, K. G. Estabrook, E. M. Campbell, C. L. Wang, D. W. Phillion, E. A. Williams, and W. L. Kruer, *Phys. Rev. Lett.* **53**, 18 (1984).
- ³⁵R. P. Drake, R. E. Turner, B. F. Lasinski, E. A. Williams, D. W. Phillion, K. G. Estabrook, W. L. Kruer, E. M. Campbell, K. R. Manes, J. S. Hildum *et al.*, *Phys. Fluids* **31**, 3130–3142 (1988).
- ³⁶S. Depierreux, D. T. Michel, V. Tassin, P. Loiseau, C. Stenz, and C. Labaune, *Phys. Rev. Lett.* **103**, 115001 (2009).
- ³⁷S. Depierreux, P. Loiseau, D. T. Michel, V. Tassin, C. Stenz, P.-E. Masson-Laborde, C. Goyon, V. Yahia, and C. Labaune, *Phys. Plasmas* **19**, 012705 (2012).
- ³⁸F. P. Condamine, N. Jourdain, D. Kramer, P. Trojek, A. Gintrand, G. Fauvel, P. Pandikian, J. Bartoníček, G. Friedman, M. Havlík *et al.*, *Plasma Phys. Controlled Fusion* **65**, 015004 (2023).
- ³⁹N. Jourdain, U. Chaulagain, M. Havlík, D. Kramer, D. Kumar, I. Majerová, V. T. Tikhonchuk, G. Korn, and S. Weber, *Matter Radiat. Extremes* **6**, 015401 (2021).
- ⁴⁰S. Weber, S. Bechet, S. Borneis, L. Brabec, M. Bučka, E. Chacon-Golcher, M. Ciappina, M. DeMarco, A. Fajstavr, K. Falk *et al.*, *Matter Radiat. Extremes* **2**, 149–176 (2017).
- ⁴¹D. H. Froula, D. Bower, M. Chrisp, S. Grace, J. H. Kamperschroer, T. M. Kelleher, R. K. Kirkwood, B. MacGowan, T. McCarville, N. Sewall *et al.*, *Rev. Sci. Instrum.* **75**, 4168 (2004).
- ⁴²F. Wasser, S. Zähler, M. Sokol, M. Rivers, S. Atzeni, F. P. Condamine, G. Cristoforetti, G. Fauvel, N. Fischer, L. A. Gizzi *et al.*, *Rev. Sci. Instrum.* **94**, 093503 (2023).
- ⁴³G. Cristoforetti, L. Antonelli, S. Atzeni, F. Baffigi, F. Barbato, D. Batani, G. Boutoux, A. Colaitis, J. Dostal, R. Dudzak *et al.*, *Phys. Plasmas* **25**, 012702 (2018).
- ⁴⁴R. P. Drake, E. A. Williams, P. E. Young, K. Estabrook, W. L. Kruer, D. S. Montgomery, H. A. Baldis, and T. W. Johnson, *Phys. Fluids* **1**, 2217–2223 (1989).
- ⁴⁵H. X. Vu, D. F. DuBois, and B. Bezzerides, *Phys. Plasmas* **14**, 012702 (2007).
- ⁴⁶B. B. Afeyan and E. A. Williams, *Phys. Fluids* **28**, 3397–3408 (1985).
- ⁴⁷H. A. Baldis, *Laser-Plasma Interactions*, Handbook of Plasma Physics, edited by A. Rubenchik and S. Witkowski (Elsevier, 1991).
- ⁴⁸C. S. Liu, M. N. Rosenbluth, and R. B. White, *Phys. Fluids* **17**, 1211 (1974).
- ⁴⁹S. Atzeni, A. Schiavi, F. Califano, F. Cattani, F. Cornolti, D. Del Sarto, T. Liseykina, A. Macchi, and F. Pegoraro, *Comput. Phys. Commun.* **169**, 153–159 (2005).
- ⁵⁰J. D. Huba, *NRL Plasma Formulary* (Naval Research Laboratory, Washington, DC, 2019).